




Article

Hydrothermally Assisted Fabrication of TiO₂-Fe₃O₄ Composite Materials and Their Antibacterial Activity

Adam Kubiak ¹, Marta Kubacka ¹, Elżbieta Gabała ², Anna Dobrowolska ³,
Karol Synoradzki ^{4,5} , Katarzyna Siwińska-Ciesielczyk ¹ , Katarzyna Czaczyk ³ and
Teofil Jesionowski ^{1,*} 

- ¹ Faculty of Chemical Technology, Institute of Chemical Technology and Engineering, Poznan University of Technology, Berdychowo 4, PL-60965 Poznan, Poland; adam.l.kubiak@doctorate.put.poznan.pl (A.K.); marta00146@wp.pl (M.K.); katarzyna.siwinska-ciesielczyk@put.poznan.pl (K.S.-C.)
- ² National Research Institute, Institute of Plant Protection, Węgorza 20, PL-60318 Poznan, Poland; elzbieta.gabala@gmail.com
- ³ Department of Biotechnology and Food Microbiology, Poznan University of Life Sciences, Wojska Polskiego 48, PL-60637 Poznan, Poland; anna.dobrowolska@up.poznan.pl (A.D.); katarzyna.czaczyk@up.poznan.pl (K.C.)
- ⁴ Institute of Molecular Physics, Polish Academy of Sciences, Smoluchowskiego 17, PL-60179 Poznan, Poland; karol.synoradzki@ifmpan.poznan.pl
- ⁵ Institute of Low Temperature and Structure Research, Polish Academy of Sciences, Okólna 2, PL-50422 Wrocław, Poland
- * Correspondence: teofil.jesionowski@put.poznan.pl; Tel.: +48-61-665-37-20

Received: 19 September 2020; Accepted: 20 October 2020; Published: 22 October 2020



Abstract: The TiO₂-Fe₃O₄ composite materials were fabricated via the hydrothermal-assisted technique. It was determined how the molar ratio of TiO₂ to Fe₃O₄ influences the crystalline structure and morphology of the synthesized composite materials. The effect of the molar ratio of components on the antibacterial activity was also analyzed. On the basis of XRD patterns for the obtained titanium(IV) oxide-iron(II, III) oxide composites, the two separate crystalline forms—anatase and magnetite—were observed. Transmission electron microscopy revealed particles of cubic and tetragonal shape for TiO₂ and spherical for Fe₃O₄. The results of low-temperature nitrogen sorption analysis indicated that an increase in the iron(II, III) oxide content leads to a decrease in the BET surface area. Moreover, the superparamagnetic properties of titanium(IV) oxide-iron(II, III) oxide composites should be noted. An important aim of the work was to determine the antibacterial activity of selected TiO₂-Fe₃O₄ materials. For this purpose, two representative strains of bacteria, the Gram-negative *Escherichia coli* and Gram-positive *Staphylococcus aureus*, were used. The titanium(IV) oxide-iron(II, III) oxide composites demonstrated a large zone of growth inhibition for both Gram-positive and Gram-negative bacteria. Moreover, it was found that the analyzed materials can be reused as antibacterial agents in three consecutive cycles with good results.

Keywords: titania; magnetite; hydrothermal method; antibacterial agents; reusability

1. Introduction

Currently, there is a significant increase in research into the design of new antimicrobial materials to control and reduce the number of microorganisms around us. Bacterial infections are a problem that affects millions of people worldwide every year. They raise both social and medical concerns [1,2]. Bacterial infections may appear in postoperative wounds if the procedure for the sterilization of the instruments and implants was not strictly followed [3]. Bacteria are capable of forming a biofilm structure, thus protecting themselves against the environment and the human immune

system [4,5]. At the implant site, an infection develops, which spreads to the whole body and may cause life-threatening complications [6,7]. To reduce the likelihood of infection, many different antibiotics are administered to patients at high doses, which may cause bacterial mutations and increase their drug resistance [8,9]. Many compounds and materials with antibacterial properties have been developed to prevent bacterial infections, including quaternary ammonium compounds [10], carbon nanotubes [11], metal ions [12], metal oxide molecules [13], and precious metal-based materials [14]. However, these antibacterial agents have disadvantages including environmental pollution, complexity, and the high cost of the production process or substrates [8]. There is consequently a need to continue to develop effective antibacterial materials.

Among the many materials with antibacterial properties, titanium(IV) oxide deserves particular attention, in view of properties such as good chemical and thermal stability, as well as photocatalytic activity [15]. The first report on the biocidal properties of TiO_2 was published in 1985 by Matsunaga et al. [16]. Subsequently, many articles have been published focusing on the inactivation of bacteria, viruses, and other pathogens, as well as cancer cells by photoactive titanium(IV) oxide [17–19]. However, the use of this material is subject to a practical limitation, namely the need to separate the material after the process and to perform its recovery [20]. Therefore, attention is paid to the synthesis of composite materials containing TiO_2 and Fe_3O_4 , which provide an opportunity to eliminate this problem. Iron(II, III) oxide is a good candidate, which, as a result of synthesis with titanium(IV) oxide by various techniques, significantly improves its properties. In addition, the material is magnetically recoverable and non-toxic and facilitates recycling after the process.

Much research has been conducted in recent years on the synthesis of iron oxides, in particular iron(II, III) oxide, as is reflected in the number of published documents in databases such as Scopus (approximately 2000 search results in 2019). This results from the fact that this material is a common ferrite with a cubic inverse spinel structure, showing good electrical and magnetic properties [21]. Thus, it is used in magnetic data media, such as audio and video media [22,23], but also in medicine as contrast media for magnetic resonance imaging [24], magnetic hyperthermia [25], magnetic cell separation [26], as well as in medical diagnostics and cancer therapy [27,28]. In addition, Fe_3O_4 is widely used in synthesis processes with other oxides such as silica, zinc, or copper oxides, because the systems obtained have a wide range of applications. Systems based on iron(II, III) oxide and silica are used, among others, in the purification of aqueous media [29,30] and in medicine [31,32]. However, materials based on iron(II, III) oxide and zinc oxide are used for improved removal of elements from watercourses [33], as catalysts [34,35], and as antibacterial agents [35,36]. The above review of the existing literature shows clearly that magnetite-based composite materials have applications in a range of scientific fields.

The available scientific literature indicated that the $\text{TiO}_2\text{-Fe}_3\text{O}_4$ systems can be used in many areas, including photocatalysis [37,38], removal of hazardous compounds from aqueous solutions [39,40], and magnetic resonance imaging [41]. A recoverable and reusable $\text{TiO}_2\text{-Fe}_3\text{O}_4$ photocatalyst was fabricated via a one-step co-precipitation method by Arabzadeh et al. [42]. To obtain the mentioned photocatalyst, nanoparticles of commercial P25 were used as a source of titanium(IV) oxide. Moreover, the fabricated material was applied in photocatalytic degradation of tartrazine. Babudurai et al. [43] used the anatase nanoparticles for the synthesis of $\text{TiO}_2\text{-Fe}_3\text{O}_4$ nanocomposite via the co-precipitation method. The obtained system was used as a photoactive material in the degradation process of Orange G. Salamat et al. [44], who obtained magnetic core-shell $\text{Fe}_3\text{O}_4@\text{TiO}_2$ nanoparticles by the two step hydrothermal method, which additionally were calcined at 400 °C. The Researchers proved that the core-shell $\text{Fe}_3\text{O}_4@\text{TiO}_2$ based materials showed high photooxidation activity in the degradation of the organic pollutant from steel industry wastewater. The core-shell materials were also synthesized by Kermani et al. [45]. The mentioned $\text{TiO}_2@\text{Fe}_3\text{O}_4$ magnetic materials were applied as a catalyst in the ozonation of catechol. The synthesis of titanium(IV) oxide-iron(II, III) oxide composites was also reported by Yuxiang et al. [46], who used the two step sol-gel method assisted by the calcination process to obtain superparamagnetic photocatalysts. Li et al. [47] indicated that the addition of graphene

oxide to $\text{TiO}_2\text{-Fe}_3\text{O}_4$ materials improved their photocatalytic properties in Vis light. Bui et al. [48] described the modification of $\text{TiO}_2\text{-Fe}_3\text{O}_4$, with magnesium amino-functionalized clay via the sol-gel method. Additionally, the authors used the obtained materials for the water treatment process realized by applying photo-Fenton and photocatalytic reactions. Beketova et al. [49] reported the application of titanium(IV) oxide nanotubes decorated with iron(II, III) oxide nanoparticles via the co-precipitation and/or solvothermal methods. The fabricated materials were used as photocatalysts in the degradation process of methylene blue.

Based on the literature review, it should be noted that the synthesis of $\text{TiO}_2\text{-Fe}_3\text{O}_4$ composites is gaining importance, due to the good photocatalytic properties of titanium(IV) oxide and the magnetic properties of iron(II, III) oxide. However, attention should be paid to the fact that, based on the review mentioned above, the titanium(IV) oxide-iron(II, III) oxide products were mainly fabricated by the co-precipitation and sol-gel methods. Moreover, many researchers used commercial titanium(IV) oxide, e.g., anatase nanoparticles and P25. Additionally, in many cases, the synthesis of the mentioned materials was multistage and assisted by the calcination process. Therefore, we decided to apply the one step hydrothermally-assisted method to obtain $\text{TiO}_2\text{-Fe}_3\text{O}_4$ materials with a well-formed crystalline structure and morphology. What is more important is that it consumes much lower energy than conventional methods and does not generate toxic waste; thanks to that, it can be an element of a strategy toward environmentally friendly production. Furthermore, although in the scientific literature, the antibacterial activities for titanium(IV) oxide and iron(II, III) oxide separately were shown, the antibacterial properties for $\text{TiO}_2\text{-Fe}_3\text{O}_4$ composites have not been widely described until now. For this reason, in this work, the antibacterial activity of the selected $\text{TiO}_2\text{-Fe}_3\text{O}_4$ composites was determined. For this purpose, two representative strains of bacteria, the Gram-negative *Escherichia coli* and Gram-positive *Staphylococcus aureus*, were used. Moreover, for the analyzed composite materials, the reusability in three consecutive cycles was determined.

2. Materials and Methods

2.1. Materials

TiCl_4 (97%), $\text{FeCl}_2\cdot 4\text{H}_2\text{O}$ (98%), $\text{FeCl}_3\cdot 6\text{H}_2\text{O}$ (97%) $\text{NH}_3\cdot \text{H}_2\text{O}$ (25%), and $(\text{CH}_3)_2\text{CHOH}$ (99.5%, IPA) were purchased from Sigma-Aldrich (St. Louis, MO, USA). The reagents used were analytical grade. Moreover, deionized water was used in all experiments.

2.2. Synthesis of $\text{TiO}_2\text{-Fe}_3\text{O}_4$ Composites

In a typical one step hydrothermally-assisted synthesis procedure, 1.5 g of $\text{FeCl}_2\cdot 4\text{H}_2\text{O}$ and 3 g of $\text{FeCl}_3\cdot 6\text{H}_2\text{O}$ (in the molar ratio $\text{Fe}^{2+}:\text{Fe}^{3+} = 1:2$) were dissolved in 100 cm^3 of deionized water. In the next step, to the obtained solution of iron(II, III) oxide precursor, a specified amount of a 10% aqueous solution of TiCl_4 was added. The $\text{TiO}_2:\text{Fe}_3\text{O}_4$ molar ratio was controlled by holding the volume of iron salts constant and varying the volume of titania precursor. The mixture was then placed on a magnetic stirrer (Ika, Werke, Staufen, Germany), and an ammonia solution was added. After the addition of a few drops of ammonia, the solution had a grey-black color. The final pH was 9–10. Then, the resulting mixture was subjected to hydrothermal treatment at $200\text{ }^\circ\text{C}$ for 12 h. The obtained titanium(IV) oxide-iron(II, III) oxide composites were separated with the use of an external magnetic field and washed with deionized water. Finally, the $\text{TiO}_2\text{-Fe}_3\text{O}_4$ materials were dried at $45\text{ }^\circ\text{C}$ for 12 h and underwent classification. For comparison, titanium(IV) oxide and iron(II, III) oxide samples were fabricated as reference samples.

2.3. Characterization of Synthesized Composites

The dispersion properties, e.g., the particle size distribution (PSD) of the synthesized composite, were analyzed using the non-invasive backscattering method applying a Zetasizer Nano ZS apparatus (Malvern Instruments Ltd., Malvern, UK).

The morphology and microstructure of the synthesized composite were investigated using an EVO40 scanning electron microscope (SEM) (Zeiss, Jena, Germany) and a Hitachi HT7700 transmission electron microscope (TEM) (Hitachi, Tokyo, Japan) operating in High-Contrast (HC) and High-Resolution (HR) modes.

To determine the crystalline structure of the fabricated products, the X-ray diffraction method was applied. The Rigaku Miniflex 600 apparatus (Rigaku, Tokyo, Japan) operating with Cu K α radiation ($\lambda = 1.5418 \text{ \AA}$) was used. The patterns were obtained over an angular range of 10–80°. The diffraction patterns were evaluated by the Rietveld method using the Fullprof software [50]. The crystallite size of the synthesized composites in the vertical direction to the corresponding lattice plane was determined using Scherrer's equation [29,30] with the constant equal to 0.891. Quantitative analysis, including phase composition with the standard deviation, was calculated using the Reference Intensity Ratio (RIR) method from the most intensive independent peak of each phase.

The low-temperature nitrogen sorption allowed determining the textural properties such as: surface area, pore volume, and pore diameter. In the above-mentioned analysis, the apparatus ASAP 2020 porosimeter (Micromeritics Instrument Co., Norcross, GA, USA) was used. Before measurement, the materials were degassed at 120 °C for 4 h. The surface area was determined by the multipoint BET method using adsorption data in the relative pressure (p/p_0) range of 0.05–0.30.

The SQUID magnetometer (MPMS-XL, Quantum Design, San Diego, CA, USA) was used to perform magnetic measurements. The temperature dependences of the magnetization were measured in a magnetic field of 0.1 T in the temperature range of 2–300 K. Magnetization loops were collected at 5 and 300 K in magnetic fields up to 5 T.

In order to identify the functional groups present on the surface of the composite materials, Fourier transform infrared spectroscopy was carried out. The FTIR spectra were measured over a wavenumber range of 4000–420 cm^{-1} using a Vertex 70 apparatus (Bruker, Leipzig, Germany).

The Jupiter STA 449 F3 apparatus (Netzsch GmbH, Bad Berneck im Fichtelgebirge, Germany) was applied to determine thermogravimetric curves. The analysis was performed under flowing nitrogen at a heating rate of 10 °C/min in a temperature range of 30–1000 °C.

2.4. Antibacterial Activity

Antibacterial tests were carried out using two methods: the agar diffusion method [51] and the standard shake flask method [52]. Both tests were performed using Gram-negative *Escherichia coli* (ATCC 10536) and Gram-positive *Staphylococcus aureus* (ATCC 33592).

For the first of the above-mentioned methods (agar diffusion), the microorganisms were grown in nutrient broth (OXOID CM 0001). The broth contained (in g/dm^3) meat extract 1.0, yeast extract 2.0, peptone 5.0, sodium chloride 5.0, glucose 20.0 and agar 15.0, respectively. The final pH of the mixture was 7.4 ± 0.2 . Moreover, the cultures of bacteria were grown at $35 \pm 2 \text{ °C}$ for 24 h. To determine the antimicrobial properties, the Muller–Hinton medium (OXOID CM 0337) was applied. This medium contained (in g/dm^3) dehydrated beef infusion 300.0, casein hydrolysate 17.5, starch 1.5, and agar 17.0 (the final pH is 7.3 ± 0.1). The plates were inoculated using indicator microorganisms in the range of 10^7 CFU/cm^3 (100 μL) and stayed for 15 min for adsorbing the microorganisms to the surface. Next, the wells (14 mm diameter) were cut in agar plates, and 0.1 g of analyzed composite: (7)TiO₂-(3)Fe₃O₄, (5)TiO₂-(5)Fe₃O₄, (3)TiO₂-(7)Fe₃O₄, were placed into the wells. Then, the plates were incubated at $35 \text{ °C} \pm 2 \text{ °C}$ for 24 h. After this time, the diameter of the inhibitory zone surrounding the discs was measured in mm. Tetracycline discs (6 mm, containing 30 μg of antibiotic) and reference samples (TiO₂ and Fe₃O₄) were applied as control samples.

For the second technique (shake flask method), frozen beads of the examined species were thawed, subcultured onto nutrient broth (OXOID CM 0001), and incubated at $35 \pm 2 \text{ °C}$ for 24 h. Cultures were centrifuged at 4500 g for 10 min, and cells were washed in deionized water. Cultures were resuspended in water and adjusted to 0.5 on the McFarland scale ($1.5 \times 10^8 \text{ CFU/cm}^3$) by the McFarland Densitometer (Biosan). For the experiments, the final concentration of bacteria was adjusted

to the level of 5.0×10^7 CFU/cm³. The composite materials—(7)TiO₂-(3)Fe₃O₄, (3)TiO₂-(7)Fe₃O₄—were sterilized by autoclaving (121 °C, 15 min), and next, zero-point-one grams of analyzed sterile oxide materials were incubated with 100 cm³ of bacterial suspensions at 37 °C and 230 rpm. The cell density of the suspensions before introducing the material and after 30, 60 and 120 min in contact with the material were determined using the pour plate method. These suspensions were decimally diluted in sterile physiological saline, plated on plate count agar, and incubated at 35 °C ± 2 °C for 24–48 h to determine the number of surviving bacteria. The materials after use were recovered with an external magnetic field and used a second and third time, to determine the stability of the antibacterial activity. The procedure for the determination of the reduction of the viability of the analyzed materials was the same as in the case of the first use.

3. Results and Discussion

3.1. Dispersion and Morphology

For any material, irrespective of its type, the dispersion properties, as well as morphology and microstructure are significant factors that affect its potential applications. In the first step, for the fabricated samples, the Particle Size Distributions (PSDs) were determined and the SEM analysis was performed (Table 1).

Table 1. PSDs and SEM images of the obtained composite and references samples.

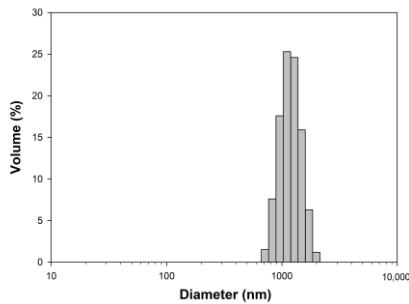
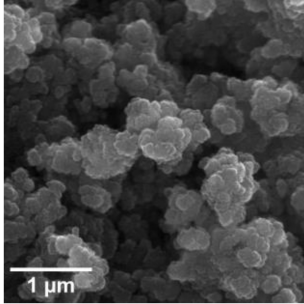
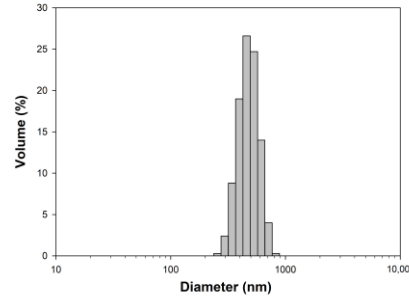
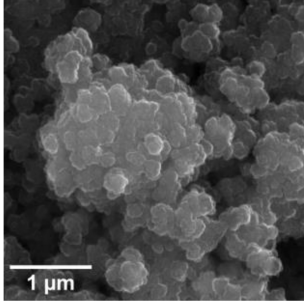
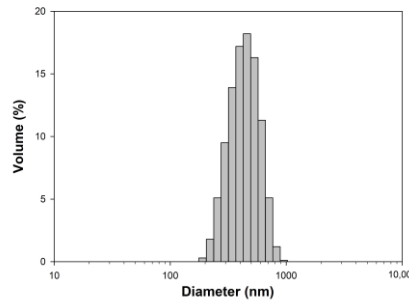
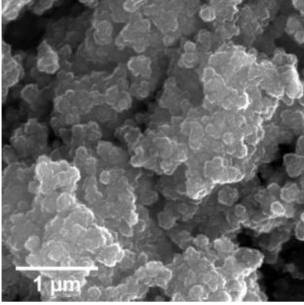
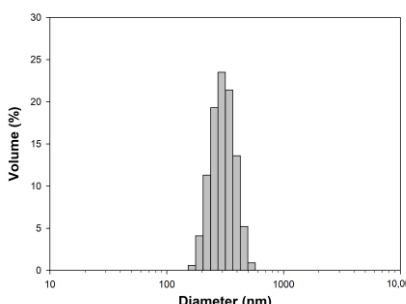
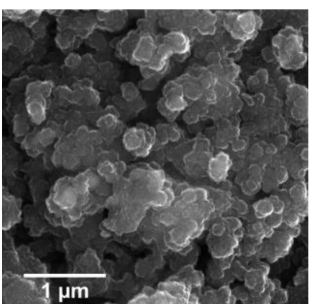
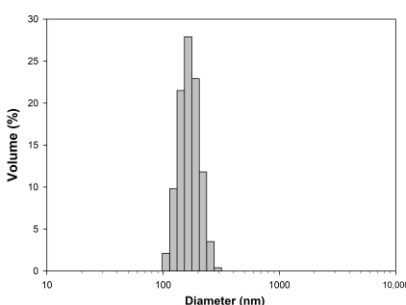
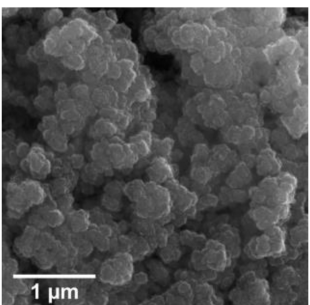
Sample	Particle Size Distributions (PSD)	SEM Images
TiO ₂		
(7)TiO ₂ -(3)Fe ₃ O ₄		
(5)TiO ₂ -(5)Fe ₃ O ₄		

Table 1. Cont.

Sample	Particle Size Distributions (PSD)	SEM Images
(3)TiO ₂ -(7)Fe ₃ O ₄		
Fe ₃ O ₄		

For the reference sample, a TiO₂ maximum volume contribution of 25.3% corresponds to agglomerates of 1106 nm in diameter. Additionally, a Polydispersity Index (PDI) of 0.142 was determined for titanium(IV) oxide. The particle size distribution of iron(II, III) oxide confirmed the presence of particles in the range of 105 to 295 nm. The maximum volume contribution (27.9%) came from particles of 164 nm in diameter. This sample had a polydispersity index equal to 0.312. Based on the presented results of the particle size distribution, it is shown that the molar ratio of TiO₂:Fe₃O₄ has a meaningful influence on the dispersion properties. The sample (7)TiO₂-(3)Fe₃O₄ obtained with a molar ratio of TiO₂:Fe₃O₄ = 7:3 contains particles in the range of 255–825 nm. The maximum volume contribution of 26.6% corresponds to agglomerates of 458 nm in diameter. Moreover, the PDI of this sample is 0.211, which indicated that the composite material is homogeneous. In the case of the sample synthesized with the equimolar ratio of TiO₂:Fe₃O₄, it contains particles in the range of 190–955 nm. The maximum volume contribution of 18.2% corresponds to agglomerates of 458 nm in diameter. Furthermore, for the material mentioned above, the PDI = 0.256 was determined; whereas, slightly smaller particles were observed in the sample (3)TiO₂-(7)Fe₃O₄, as confirmed by their diameter range of 164–531 nm and by the dominant diameter (295.3 nm). It should be noted that the analyzed composite is relatively homogeneous, as indicated by the low value of the polydispersity index (0.289). Based on the dispersion analysis, it was confirmed that increasing the content of Fe₃O₄ in the synthesized composites leads to products with smaller particles. Moreover, it should be noted that all binary materials have a monomodal particle size distribution, as well as a high tendency to agglomerate.

In the next step of physicochemical characterization, scanning electron microscopy was applied to evaluate the morphology of the synthesized TiO₂-Fe₃O₄ systems. The presented SEM pictures indicate the effect of the molar ratio of the components on the morphology of the products. Moreover, it was shown that for all analyzed materials, the tendency to agglomerate is observed. However, increasing the contribution of iron(II, III) oxide causes smaller aggregates. The results obtained by scanning electron microscopy correspond with the dispersion analysis. Furthermore, to determine the shape of the TiO₂ and Fe₃O₄ phases, TEM analysis was carried out (Figure 1).

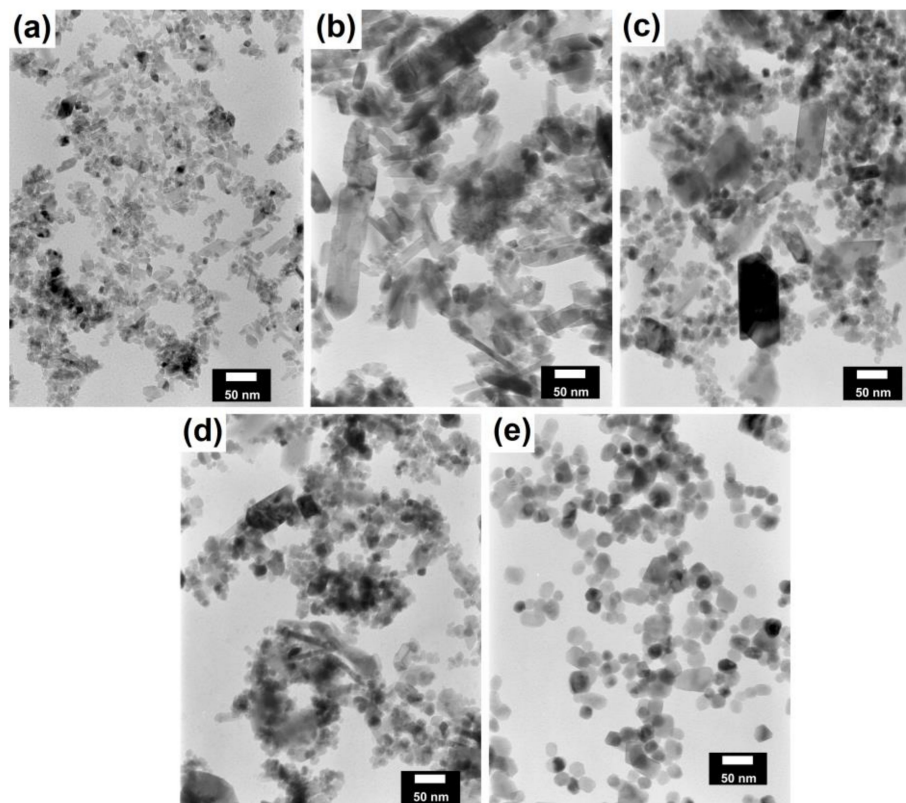


Figure 1. TEM images for composite materials and reference samples: (a) TiO_2 ; (b) $(7)\text{TiO}_2-(3)\text{Fe}_3\text{O}_4$; (c) $(5)\text{TiO}_2-(5)\text{Fe}_3\text{O}_4$; (d) $(3)\text{TiO}_2-(7)\text{Fe}_3\text{O}_4$; (e) Fe_3O_4 .

In the TEM images for TiO_2 and Fe_3O_4 , we can observe typical nanoparticles (diameter <50 nm), being in agreement with the theory of Karatutlu and co-authors [53], on the formation of nanoparticles in the liquid phase. Titanium(IV) oxide particles of a cubic and tetragonal shape with a diameter of about 25 nm are shown. For iron(II, III) oxide, a spherical particle shape with a diameter in the range of 10–20 nm was observed. Subsequently, the titanium(IV) oxide-iron(II, III) oxide composites were examined. For all of the synthesized composites, the same shape of particles as for the reference samples was observed. Moreover, particles with a rod-like structure were also noted. The presence of the structure mentioned above can be associated with impurities or the unreacted substrate during synthesis, e.g., FeOOH . For the precise characterization of composite materials, HR-TEM and mapping by EDS were carried out. Both above-mentioned analyses were performed for selected samples: $(7)\text{TiO}_2-(3)\text{Fe}_3\text{O}_4$ and $(3)\text{TiO}_2-(7)\text{Fe}_3\text{O}_4$.

EDS mapping enabled the determination of the distribution of the analyzed elements (titanium, oxygen, and iron) in the synthesized composite materials. The EDS maps of the selected materials are shown in Figures 2 and 3.

Based on the obtained results, it is indicated that the distribution of titanium(IV) oxide and iron(II, III) oxide is not homogeneous for the analyzed composites. Furthermore, both analyzed elements: titanium and iron are in larger aggregates of nanoparticles. However, it should be noted that the localization of titanium and iron elements may indicate the occurrence of surface interactions between components in composite systems.

Transmission electron microscopy in high-resolution mode was used to determine crystallographic spacings and planes. The results of HR-TEM are shown in Figures 4 and 5.

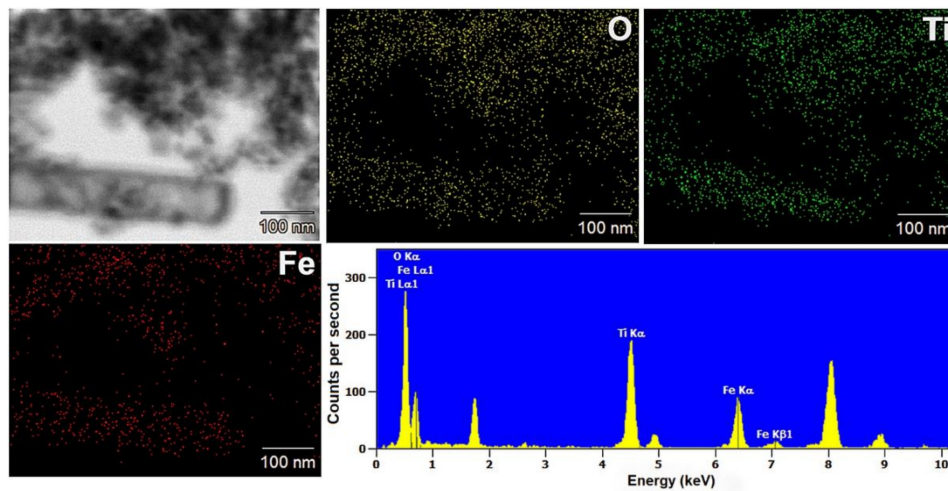


Figure 2. Results of EDS mapping for the (7)TiO₂-(3)Fe₃O₄ composite.

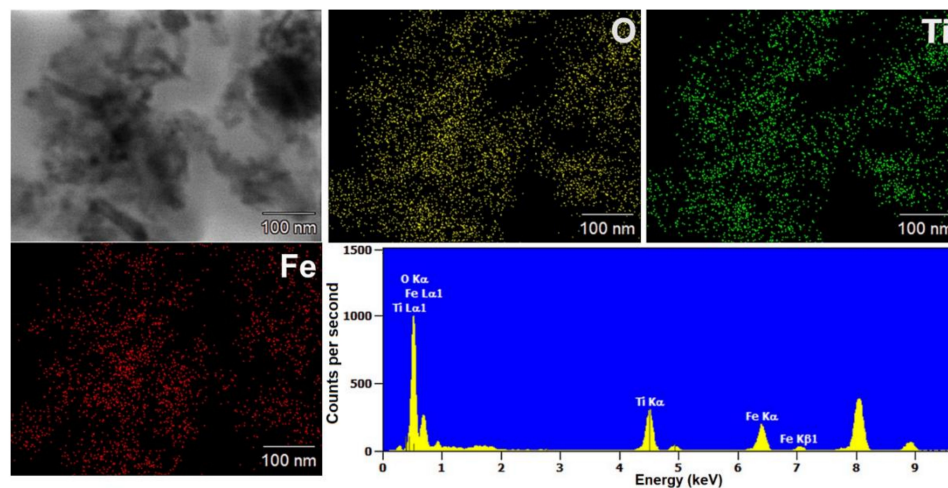


Figure 3. Results of EDS mapping for the (3)TiO₂-(7)Fe₃O₄ composite.

According to previously reported results for the (7)TiO₂-(3)Fe₃O₄ composite, the crystallographic spacings of 0.24 nm and 0.35 nm, characteristic of the anatase phase, were observed [54]. Moreover, the angle in the crystallographic lattice is 111.5°. In Figure 5, the crystallographic lattice parameters characteristic for magnetite are noted. Spacings equal to 0.24 nm and 0.45 nm characteristic for planes (111) and (311) in the Fe₃O₄ phase were observed [55]. Very similar results were obtained for the second analyzed titanium(IV) oxide-iron(II, III) oxide composite, (3)TiO₂-(7)Fe₃O₄. On this basis, it was concluded that regardless of the TiO₂:Fe₃O₄ molar ratio, these materials exhibit the same crystalline lattice parameters as indicated by the HR-TEM analysis presented above. However, the interactions between iron(II, III) oxide and titanium(IV) oxide should also be described. Based on available scientific knowledge, it was concluded that the incorporation of magnetite particles on titania involves only surface junctions, because we did not observe a mixed crystalline structure, for example ilmenite (FeTiO₃) or others. It should be noted, however, that the main objective of the presented research is not to fabricate a mixed crystalline structure of titania and iron oxide, but composites with a stable junction between these two components, which was confirmed by the conducted EDS analyses: coverage of EDS maps for titanium and iron. Furthermore, attention should be paid to the fact that both TiO₂ and Fe₃O₄ occur in the form of aggregated nanoparticles; therefore, the surface-junction is possible, because both phases (TiO₂ and Fe₃O₄) surround each other, which was observed in the presented TEM and HR-TEM images.

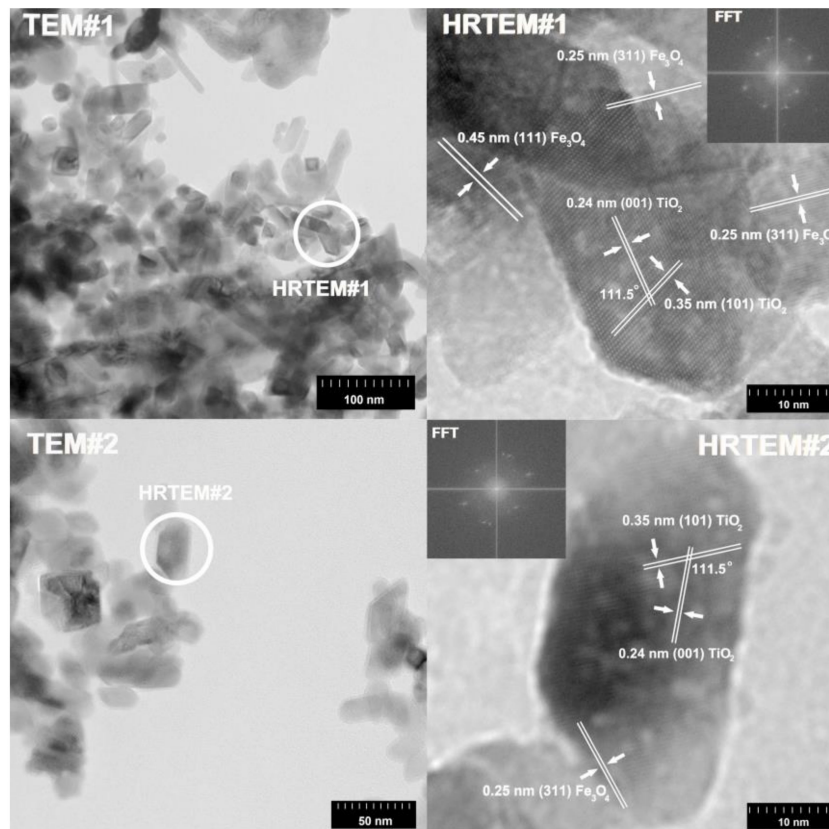


Figure 4. TEM, HR-TEM, and FFT results for the (7)TiO₂-(3)Fe₃O₄ sample.

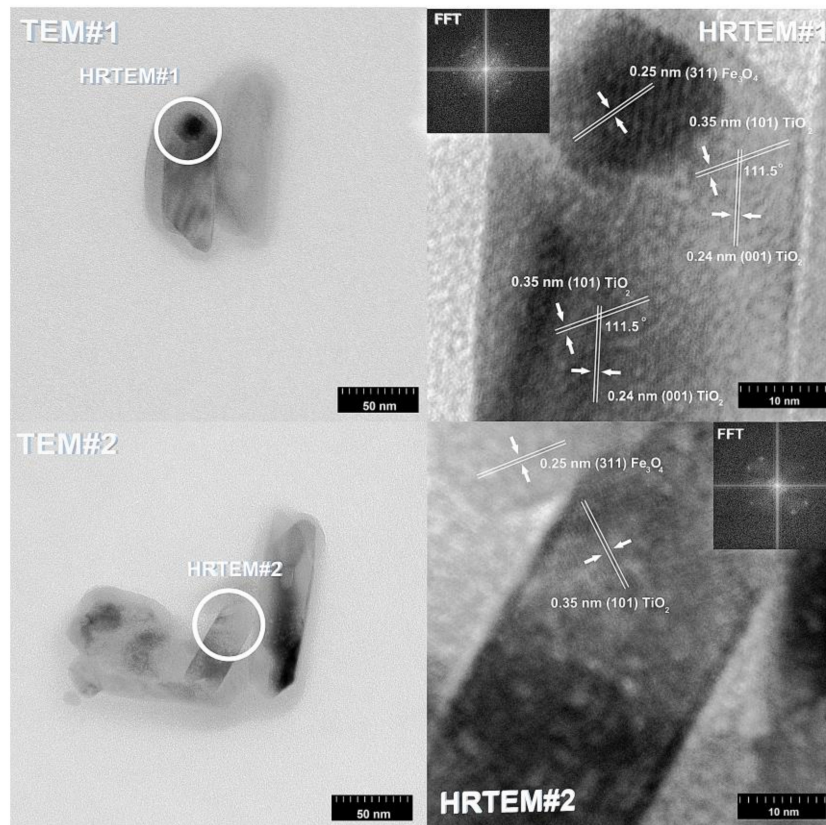


Figure 5. TEM, HR-TEM, and FFT results for the (3)TiO₂-(7)Fe₃O₄ sample.

3.2. Crystalline Structure

The XRD analysis was performed to examine whether the obtained materials have a defined crystal structure. The patterns of the synthesized composite materials and reference samples are presented in Figure 6a. For all samples, a set of distinct reflections indicates the highly crystalline nature of the obtained materials. Moreover, the observed peaks can be assigned to the anatase phase (space group $I4_1/amd$, No. 141) and/or magnetite Fe_3O_4 (space group $Fd\bar{3}m$, No. 227) phases. For TiO_2 , the following crystallographic planes were determined: (101), (103), (104), (112), (200), (105), (211), (204), (116) (220), (215). The planes determined for magnetite were as follows: (111), (220), (311), (222), (400), (422), (333), (440), (622). The intensity of the mentioned peaks changes successively as the content of samples changes. For some composite samples (e.g., (5) TiO_2 -(5) Fe_3O_4), we observed a few additional peaks (marked with diamonds in Figure 6a) originating from the α - $FeOOH$ impurity phase (space group $Pbnm$, No. 62).

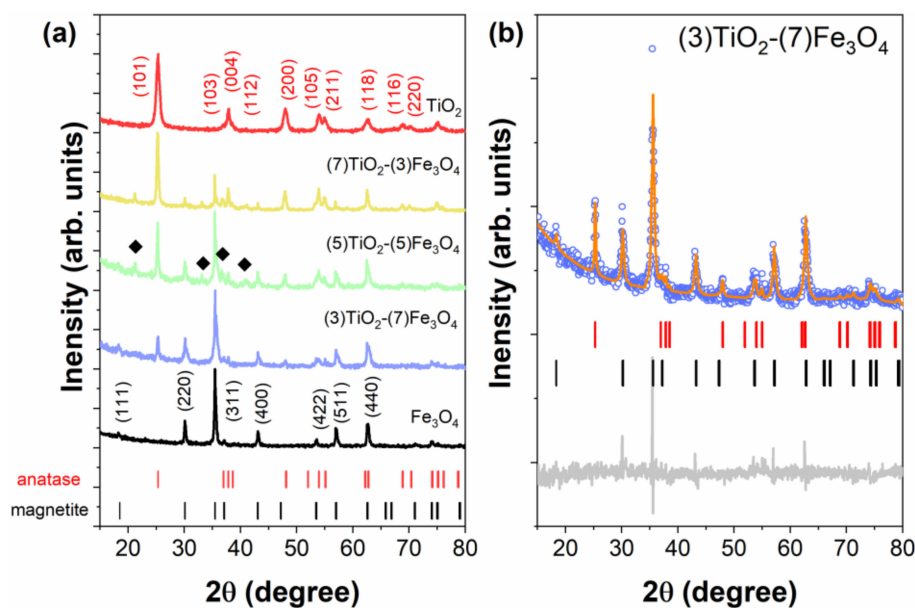


Figure 6. XRD patterns for all studied TiO_2 - Fe_3O_4 composites and reference samples (a). Peaks marked by diamonds belong to the α - $FeOOH$ impurity phases. For the most pronounced peaks, Miller indices are given. (b) XRD pattern (open circles) and Rietveld refinement (solid orange line) for the selected (3) TiO_2 -(7) Fe_3O_4 composite sample. The difference curve of the experimental and calculated intensity is shown at the bottom. The upper and lower ticks represent Bragg positions corresponding to the anatase and magnetite phases, respectively.

The mass fraction and lattice parameters values for each phase were determined according to Rietveld refinement and are summarized in Table 2. An exemplary Rietveld refinement of the XRD pattern recorded at room temperature for the (3) TiO_2 -(7) Fe_3O_4 sample is shown in Figure 6b. The calculated phase composition is in good agreement with the nominal one. It should also be noted that the lattice parameters for the composite materials and reference samples are comparable and fit well to data already published for similar systems [54,55].

Table 2. Lattice parameters, phase composition, and average crystalline size for TiO₂-Fe₃O₄ composite materials.

Sample	Lattice Parameters			Phase Composition (wt.%)		D (nm)	
	Anatase		Magnetite	Anatase	Magnetite	Anatase	Magnetite
	a (Å)	c (Å)	a (Å)				
TiO ₂	3.7937(7)	9.510(2)	-	100	-	15.3(1)	-
(7)TiO ₂ -(3)Fe ₃ O ₄	3.796(1)	9.513(2)	8.395(2)	79(2)	21(1)	24.1(2)	23.3(5)
(5)TiO ₂ -(5)Fe ₃ O ₄	3.800(1)	9.519(6)	8.382(1)	42(2)	58(2)	25.4(1)	24.3(2)
(3)TiO ₂ -(7)Fe ₃ O ₄	3.794(2)	9.508(8)	8.373(2)	19(1)	81(2)	24.9(3)	25.4(4)
Fe ₃ O ₄	-	-	8.3883(6)	-	100	-	26.1(1)

The average crystallite size (D) characteristic for the anatase and magnetite phases was calculated using Scherrer's equation ($D = K\lambda/(B\cos\theta)$) and the obtained results are presented in Table 2. The average size of the crystallites is around ~25 nm, for both the TiO₂ and Fe₃O₄ phases, in almost all samples. Only for pure TiO₂ are the crystallites smaller ($D \sim 15$ nm). The crystallite values are smaller than the particle size determined by TEM measurements, as the particles may consist of many crystallites.

Based on previous work by members of the research team, such as Jędrzak et al. [56], who synthesized superparamagnetic nanoparticles of Fe₃O₄, and Siwińska-Ciesielczyk et al. [57,58], who fabricated titania nanoparticles using different methods, it was attempted to obtain TiO₂-Fe₃O₄ materials with well-defined crystallinity using a hydrothermally-assisted method. In the literature reports, among others, Tan et al. [59] described the application of Fe₃O₄@TiO₂ materials in the sorption of uranium. However, because of the good sorption properties of the materials used (high surface area), the crystalline structure was not well formed. Khashan et al. [60] synthesized Fe₃O₄@TiO₂ nanoparticles via the co-precipitation method. The crystalline structure of the described materials indicated a well-formed anatase structure, but only single diffraction peaks derived from Fe₃O₄. A different crystalline structure was described by Zhu et al. [61], who synthesized Fe₃O₄/TiO₂ nanoparticles via a three step process. The crystallinity of the obtained materials showed diffraction bands derived from anatase, rutile, and cubic magnetite. Of course, many other researchers have described similar magnetic materials with a core-shell structure, e.g., Chen et al. [62].

3.3. Parameters of the Porous Structure

To determine the parameters of the porous structure of the fabricated composites, the low-temperature nitrogen sorption was carried out. The obtained results are presented in Table 3 and in Figure 7, respectively.

Table 3. Parameters of the porous structure for the obtained TiO₂-Fe₃O₄ materials and reference samples.

Sample	A _{BET} (m ² /g)	V _p (cm ³ /g)	S _p (nm)
TiO ₂	107	0.284	9
(7)TiO ₂ -(3)Fe ₃ O ₄	75	0.337	18
(5)TiO ₂ -(5)Fe ₃ O ₄	65	0.335	19
(3)TiO ₂ -(7)Fe ₃ O ₄	59	0.334	21
Fe ₃ O ₄	37	0.317	34

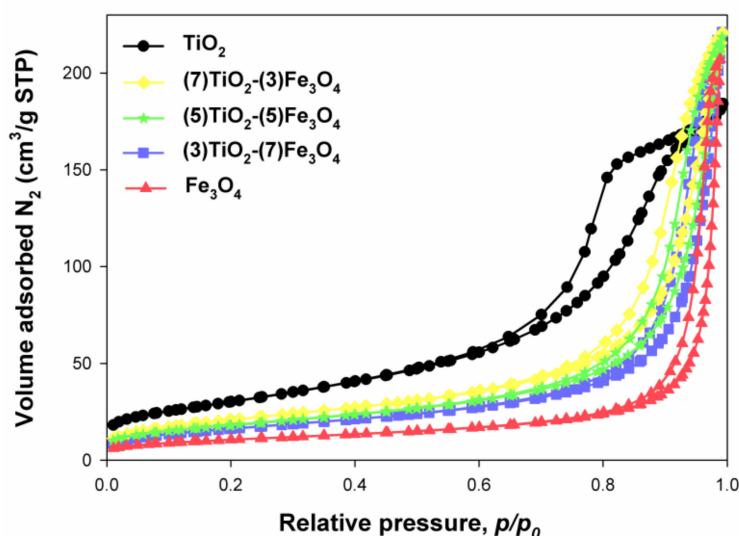


Figure 7. N_2 adsorption/desorption isotherms of TiO_2 - Fe_3O_4 composites and reference samples.

The reference sample of titanium(IV) oxide had the higher BET surface area among the studied materials ($107 \text{ m}^2/\text{g}$). Moreover, the pore volume and pore diameter for TiO_2 were respectively $0.284 \text{ cm}^3/\text{g}$ and 9 nm . The iron(II, III) oxide was found to have a BET surface area of $37 \text{ m}^2/\text{g}$, a pore volume of $0.317 \text{ cm}^3/\text{g}$, and a pore diameter of 34 nm . The $(7)TiO_2$ - $(3)Fe_3O_4$ sample had a BET surface area of $75 \text{ m}^2/\text{g}$, with a pore diameter and pore volume of 18 nm and $0.337 \text{ cm}^3/\text{g}$. For the titanium(IV) oxide-iron(II, III) oxide composite obtained at an equimolar ratio, the values were $A_{BET} = 65 \text{ m}^2/\text{g}$, $V_p = 0.335 \text{ cm}^3/\text{g}$, and $S_p = 19 \text{ nm}$. For the system with a molar ratio $TiO_2:Fe_3O_4 = 3:7$, the BET surface area was $59 \text{ m}^2/\text{g}$, the pore diameter 21 nm , and the pore volume $0.334 \text{ cm}^3/\text{g}$.

Comparing the results obtained for TiO_2 - Fe_3O_4 materials with the available literature, we should take note of the study by Feizpoor et al. [63], who obtained a TiO_2 - Fe_3O_4 system by heating at the boiling point under a reflux condenser. For the material with a molar ratio $TiO_2:Fe_3O_4 = 4:1$, a BET surface area of $17 \text{ m}^2/\text{g}$ was obtained, with a pore diameter of 49.2 nm and a pore volume of $0.2 \text{ cm}^3/\text{g}$. Shojei et al. [64] synthesized materials based on titania and magnetite using the sol-gel method. The resulting system had a surface area of $160 \text{ m}^2/\text{g}$ and a pore volume of $0.34 \text{ cm}^3/\text{g}$. Li et al. [65], who synthesized a material containing TiO_2 and Fe_3O_4 by an alkaline hydrothermal etching-assisted crystallization method, reported the BET surface area of the obtained system to be $187 \text{ m}^2/\text{g}$. Shojaie et al. [66] obtained TiO_2 - Fe_3O_4 -Ag ternary systems by an ultrasonic method supported by a hydrothermal method. For a sample containing 0.5 g of TiO_2 , 0.05 g of Fe_3O_4 , and 2 g of Ag, the BET surface area was $45 \text{ m}^2/\text{g}$, the pore volume $0.3 \text{ cm}^3/\text{g}$, and the pore diameter 14.02 nm . Fisli et al. [67] synthesized TiO_2 - Fe_3O_4 materials using heteroagglomeration. For a material with a molar ratio $TiO_2:Fe_3O_4 = 1:0.5$, the BET surface area was $91 \text{ m}^2/\text{g}$. However, for samples obtained with the ratio of titanium(IV) oxide to iron(II, III) oxide equal to $1:1$ and $1:2$, the respective BET surface areas were $64 \text{ m}^2/\text{g}$ and $57 \text{ m}^2/\text{g}$.

3.4. Magnetic Properties

All magnetic properties of titanium(IV) oxide-iron(II, III) oxide composites are summarized in Figure 8. As inferred from this figure, all prepared materials revealed similar magnetic properties as pure nano- Fe_3O_4 . The temperature dependence of magnetization (Figure 8a) shows a strong bifurcation of the Zero-Field-Cooling (ZFC) [68] curve and Field-Cooled (FC) curve. A kink in both the ZFC and FC curves at $\sim 120 \text{ K}$ is related to the Verwey transition [69]. The temperature at which this structural transition occurs (T_V) is stoichiometry [70], shape [71], and size dependent [72]. As the addition of the TiO_2 does not change the T_V , we conclude that the size and chemical composition of magnetite particles are conserved, which manifests the high quality of our samples. In $M(T)$ relationships, there is

no clear trace of blocking temperature (T_B), which usually manifests itself as a wide maximum in the ZFC curve. Part (b) of the Figure 8 shows magnetization loops. At RT, there is no sign of magnetic hysteresis and remanence. However, at 5 K (inset of Figure 8b), we observe a clear hysteresis loop for all magnetite-based materials. The magnetization saturation value (M_s) of pure Fe_3O_4 is 73.7(5) emu/g, and it is smaller than for bulk magnetite, which may result from spin disorder, variations in crystallinity, or antiphase domain boundaries [73]. With the addition of TiO_2 [74], which is paramagnetic, the M_s value drops. All results indicate superparamagnetic-like behavior for all samples containing Fe_3O_4 . However, the absence of a clear anomaly for the blocking phenomenon in $M(T)$ curves and the relatively large size of Fe_3O_4 particles (>25/50 nm) could suggest that our materials are rather the ferromagnetic monodomain than superparamagnetic [75,76]. Nevertheless, at RT, all prepared composite materials can be easily separated from water solution by a permanent magnet, as is demonstrated in the inset of Figure 8a.

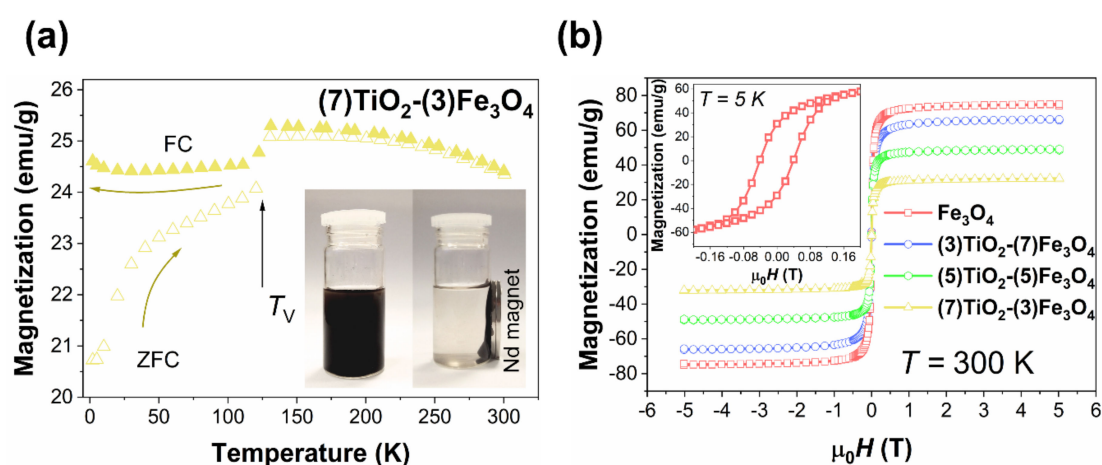


Figure 8. Magnetic properties of $\text{TiO}_2\text{-Fe}_3\text{O}_4$ composites: (a) Magnetization of selected composite vs. temperature. The inset shows magnetic separation of $\text{TiO}_2\text{-Fe}_3\text{O}_4$ composites suspended in water. (b) Magnetization vs. external magnetic field. The inset shows the magnetic loop for pristine Fe_3O_4 at 5 K.

3.5. FTIR Spectroscopy

In order to identify the functional groups present on the surface of the composite materials and reference samples, Fourier transform infrared spectroscopy was carried out. The FTIR spectra for the reference samples and $\text{TiO}_2\text{-Fe}_3\text{O}_4$ materials are shown in Figure 9.

In the FTIR spectrum for the TiO_2 reference sample, the stretching vibrations of the $-\text{Ti}\equiv\text{O}$ group (715 cm^{-1}) [77] were observed. For the Fe_3O_4 reference sample, the band occurring at 595 cm^{-1} corresponds to stretching vibrations of Fe-O [9]. Furthermore, for all fabricated materials, the stretching (3400 cm^{-1}) [78] and bending (1600 cm^{-1}) [79] vibrations corresponding to the hydroxyl group ($-\text{OH}$) were noted. The FTIR spectra for the $\text{TiO}_2\text{-Fe}_3\text{O}_4$ materials contained bands characteristic for both TiO_2 and Fe_3O_4 , as well as additional bands for the stretching (3145 cm^{-1}) and bending (1400 cm^{-1}) vibrations of the N-H groups, derived from ammonia, which was the pH regulator in the synthesis. Moreover, it should be noted that the TiO_2 and Fe_3O_4 bands are very close on the FTIR spectra; for this reason, the $\text{Ti}=\text{O}$ band for the sample $(3)\text{TiO}_2\text{-(7)Fe}_3\text{O}_4$ is not visible.

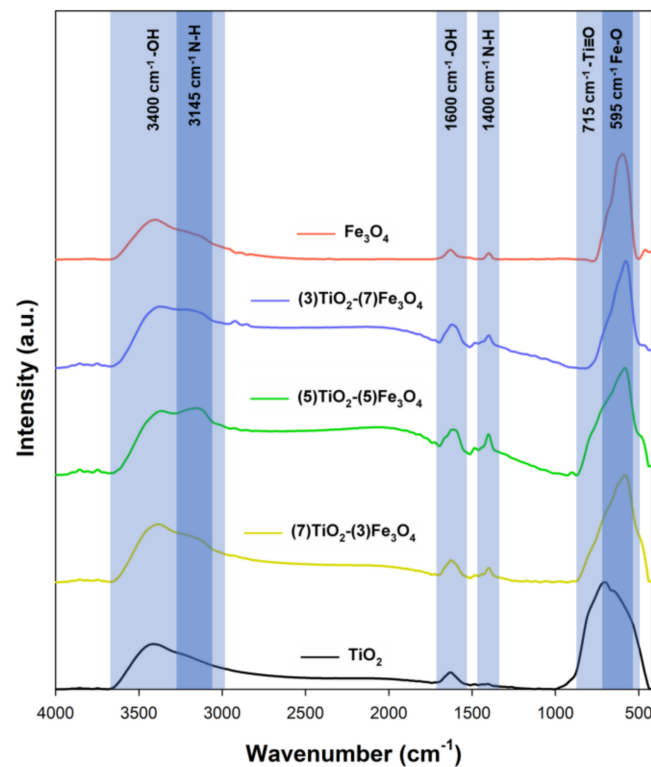


Figure 9. FTIR spectra for the TiO_2 , Fe_3O_4 , and $\text{TiO}_2\text{-Fe}_3\text{O}_4$ materials.

3.6. Thermal Analysis

Thermal stability is a significant physicochemical parameter, which can enable the potential use of composite materials. The thermal stability of the synthesized materials was evaluated using TGA analysis (Figure 10).

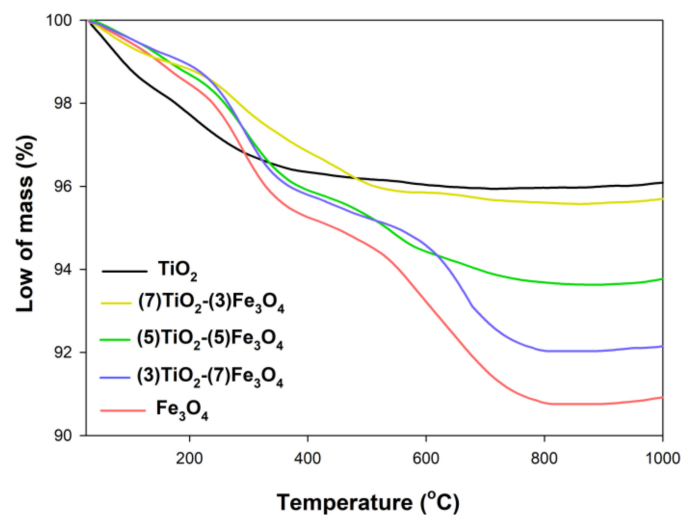


Figure 10. TGA curves for the $\text{TiO}_2\text{-Fe}_3\text{O}_4$ materials and reference samples.

The total decrease in mass for the titanium(IV) oxide sample was 3.8%, which was bound up with the elimination of bound surface H_2O (in a temperature range of 0–400 °C). Similar observations were made by Chan et al. [80], who observed a total decrease in mass for a sample equal to 20% with the removal of bound surface water in the temperature range of 0–300 °C. Three mass decreases were observed for the Fe_3O_4 reference sample, in the temperature ranges of 0–250 °C (2.5%), 300–600 °C

(2.5%), and 600–800 °C (1.4%), attributed respectively to the evaporation of water and to phase transformations from magnetite to maghemite and from maghemite to hematite. Jędrzak et al. [81] obtained particles of magnetite, which also exhibited good thermal stability; the total weight loss for that material was approximately 10%. For the (7)TiO₂-(3)Fe₃O₄ composite, the TGA curve is similar to that observed for the TiO₂ reference sample, with the total mass decrease in this case amounting to 4.5%. In the case of products fabricated with molar ratios of TiO₂:Fe₃O₄ = 5:5 and 3:7, three mass decreases were observed, resulting from the removal of surface water, the phase transitions from magnetite to maghemite and maghemite to hematite, where the total weight loss for these materials was 5.4% and 7.9%, respectively. All analyzed systems had good thermal stability up to 1000 °C, which is in accordance with the available scientific reports [43].

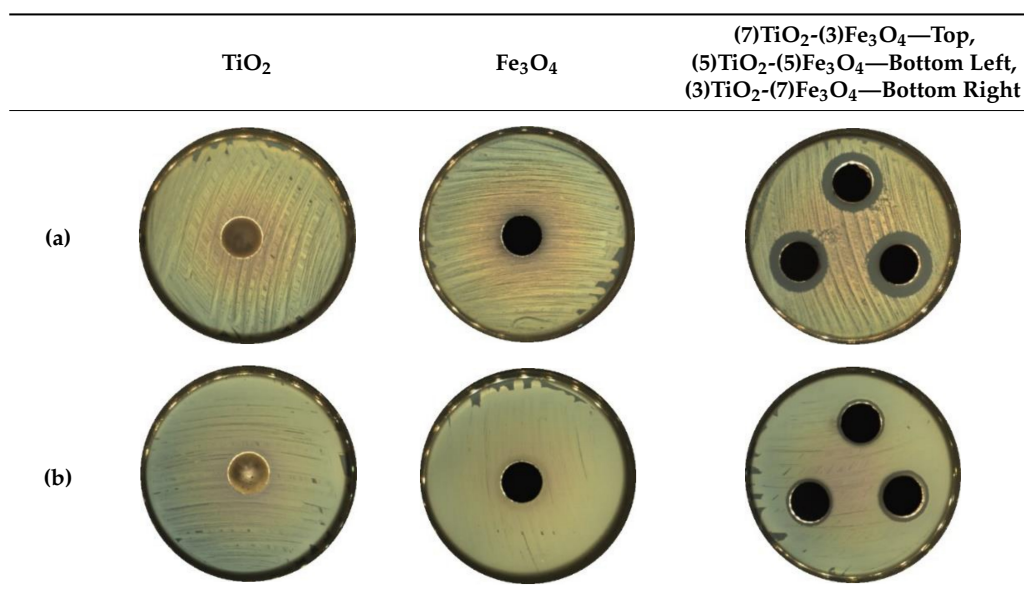
3.7. Antibacterial Properties

The antibacterial activity of (7)TiO₂-(3)Fe₃O₄, (5)TiO₂-(5)Fe₃O₄, and (3)TiO₂-(7)Fe₃O₄ materials was evaluated against representative strains of bacteria, Gram-negative *Escherichia coli*, and Gram-positive *Staphylococcus aureus*. The results of antimicrobial activity testing using the agar diffusion method are shown in Tables 4 and 5. The analyzed materials (7)TiO₂-(3)Fe₃O₄, (5)TiO₂-(5)Fe₃O₄, and (3)TiO₂-(7)Fe₃O₄ indicated a high zone of inhibition, which proved their good antibacterial activity against Gram-positive *Staphylococcus aureus* (≥ 21.0 mm) in the absence of the activity of oxides (TiO₂, Fe₃O₄) and the weak action of tetracycline (positive control). Lesser activity of the tested composites was observed in the case of *Escherichia coli* (zone of inhibition between 15 and 18 mm) with high effectiveness of the antibiotic against this bacteria.

Table 4. The zone of inhibition of the tested TiO₂-Fe₃O₄ composite materials and control samples.

Sample	Zone of Inhibition (mm)	
	<i>S. aureus</i>	<i>E. coli</i>
TiO ₂	0	0
Fe ₃ O ₄	0	0
(7)TiO ₂ -(3)Fe ₃ O ₄	21.33 (± 0.58)	15.33 (± 0.58)
(5)TiO ₂ -(5)Fe ₃ O ₄	21.00 (± 0.0)	15.67 (± 0.58)
(3)TiO ₂ -(7)Fe ₃ O ₄	23.00 (± 0.0)	17.67 (± 0.58)
tetracycline	6.33 (± 0.29)	24.67 (± 0.58)

Table 5. Zone of inhibition for *Staphylococcus aureus* (a) and *Escherichia coli* (b): agar diffusion method.



To check the antimicrobial activity of the tested materials in subsequent applications, (7)TiO₂-(3)Fe₃O₄ and (3)TiO₂-(7)Fe₃O₄ composites were selected, and the shake flask method was used. During the experiments (120 min, three cycles), the number of bacteria cells in solution without any material was monitored (control). The tested material showed high antibacterial activity against both examined strains. Samples (7)TiO₂-(3)Fe₃O₄ and (3)TiO₂-(7)Fe₃O₄ destroyed the Gram-negative *Escherichia coli* in 30 min and kept these properties during the second and third use (Figure 11). The use of (7)TiO₂-(3)Fe₃O₄ and (3)TiO₂-(7)Fe₃O₄ against Gram-positive *Staphylococcus aureus* caused the reduction of the number of bacteria for about 1, 4, and 5 log cycles after 30, 60, and 120 min of the experiment, respectively. The second and third use of the analyzed materials against *Staphylococcus aureus* indicated that they were still active. During the second use of the analyzed materials, the reduction of the amounts of bacteria was at the level of two log cycles. The material (3)TiO₂-(7)Fe₃O₄ used for the third time had similar properties as when it was used for the first time.

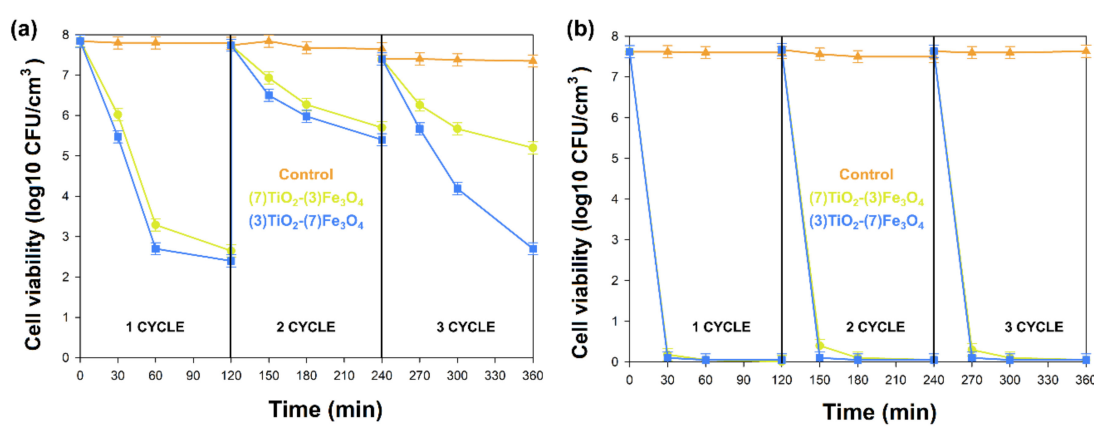


Figure 11. Antibacterial activity of examined materials during three cycles against *Staphylococcus aureus* (a) and *Escherichia coli* (b).

The antibacterial activity of metal oxides and their hybrids, including TiO₂ and Fe₃O₄ nanoparticles, has been the subject of much scientific research [82–84]. The creation of the structure TiO₂/Fe₃O₄ may enhance these properties, especially when activated by different forms of light [85–87]. Furthermore, the heterostructures TiO₂/Fe₃O₄ with other compounds (mostly gold or silver compounds) gave positive results in terms of antimicrobial growth action [88,89]. The antimicrobial effect of such a composite is connected with lipid peroxidation due to the interaction between the membrane and reactive oxygen species (ROS) [89]. The succession of this killing mechanism is the degradation of the cell wall and cytoplasmic membrane, leading to the leakage of cellular contents and cell lysis [90].

The antimicrobial effect of the (7)TiO₂-(3)Fe₃O₄, (5)TiO₂-(5)Fe₃O₄, and (3)TiO₂-(7)Fe₃O₄ materials was investigated with Gram-negative and Gram-positive, commonly used for the examination of the antibacterial activity of various materials. Two methods of testing the antibacterial properties were used in these investigations: the agar diffusion method and the standard shake flask method. In both methods, the tested materials indicated antibacterial activity against Gram-negative *Escherichia coli* and Gram-positive *Staphylococcus aureus* (Tables 4 and 5 and Figure 11). It is well known that the destruction of the outer membrane and cell wall of bacteria is crucial for bacterial cell death. The Gram-negative and Gram-positive bacteria have many differences in the structure of the membranes and cell wall. *Escherichia coli* has an outermost lipopolysaccharide layer, a thinner peptidoglycan layer (15–20 nm, in comparison to *Staphylococcus aureus* 20–80 nm), and a phospholipid bilayer (monolayer in *Staphylococcus aureus*) [91–93]. The different antibacterial mechanism of Fe₃O₄-TiO₂ nanosheets against *Escherichia coli* and *Staphylococcus aureus* was also investigated by Ma et al. [87] using SEM analysis. Before the experiments, *Escherichia coli* exhibited intact and smooth membranes and a normal elongated morphology, but already after 15 min of exposure, the cells became deformed. However,

for *Staphylococcus aureus*, no obvious cell wall and membrane destruction was noticed during the whole time of the investigations, and the cell shape changed from a regular sphere to an irregular shape. Furthermore, *Staphylococcus aureus* had a smaller diameter compared with *Escherichia coli*, and its cell surface was too small to be covered by the examined nanoparticles.

The particularly important results obtained in our investigations are connected with the second and third use of the nanoparticles of (7)TiO₂-(3)Fe₃O₄ and (3)TiO₂-(7)Fe₃O₄ and the absence of the decrease in their antibacterial activity. These properties of the obtained particles have potential applications for the environment, the biomedical field, pharmaceuticals, and other commercial productions.

4. Conclusions

Based on the experience of the research team, hydrothermally-assisted synthesis was used to obtain TiO₂-Fe₃O₄ composite materials. In a typical one-step hydrothermal synthesis procedure, highly crystalline materials were obtained. Based on the morphological analysis, the rod-like and cubic particle shape for titanium(IV) oxide and spherical shape for iron(II, III) oxide were observed. Additionally, all of the prepared composite samples exhibited superparamagnetic-like behavior.

It should be noted that the proposed hydrothermally-assisted method allowed synthesizing the TiO₂-Fe₃O₄ systems, which exhibited good antibacterial activity against *Staphylococcus aureus* and *Escherichia coli*. A key element of the study was the testing of the reusability of titanium(IV) oxide-iron(II, III) oxide composites as antibacterial agents. These experiments indicated the retention of good antibacterial activity over three successive cycles. Furthermore, the obtained TiO₂-Fe₃O₄ materials demonstrated similar or better antibacterial activity compared with the reference titanium(IV) oxide and iron(II, III) oxide samples. A possible mechanism of the antibacterial action is the destruction of the outer membrane and cell wall of the bacteria, which leads to the death of the bacterial cell. The results of the tests of antibacterial activity indicated that the synthesized TiO₂-Fe₃O₄ composite can find applications for the environment, the biomedical field, pharmaceuticals, and other commercial productions.

Author Contributions: A.K.: research concept and characterization of materials, writing the original document; M.K.: synthesis of materials; E.G.: HR-TEM and EDS analysis; A.D. and K.C.: determination of antibacterial activity and interpretation of the results; K.S.: participation in the analysis and interpretation of the magnetic properties; K.S.-C., BET analysis; K.S.-C. and T.J.: results' interpretation, critical revision, and supervision of all aspects of the research. All authors read and agreed to the published version of the manuscript.

Funding: This research was funded by the Polish Ministry of Science and Higher Education Research Grant No. 0912/SBAD/2006.

Conflicts of Interest: The authors declare no conflict of interest.

References

1. Ma, W.; Zhang, T.; Li, R.; Niu, Y.; Yang, X.; Liu, J.; Xu, Y. Bionzymatic synergism of vanadium oxide nanodots to efficiently eradicate drug-resistant bacteria during wound healing in vivo. *J. Colloid Interface Sci.* **2020**, *559*, 313–323. [[CrossRef](#)] [[PubMed](#)]
2. Han, D.; Han, Y.; Li, J.; Liu, X.; Wai, K.; Yeung, K.; Zheng, Y.; Cui, Z.; Yang, X.; Liang, Y.; et al. Enhanced photocatalytic activity and photothermal effects of Cu-doped metal-organic frameworks for rapid treatment of bacteria-infected wounds. *Applied Catal. B Environ.* **2020**, *261*, 118248. [[CrossRef](#)]
3. Sun, J.; Fan, Y.; Zhang, P.; Zhang, X.; Zhou, Q.; Zhao, J.; Ren, L. Self-enriched mesoporous silica nanoparticle composite membrane with remarkable photodynamic antimicrobial performances. *J. Colloid Interface Sci.* **2020**, *559*, 197–205. [[CrossRef](#)] [[PubMed](#)]
4. Szyszka, K.; Rewak-Soroczynska, J.; Dorotkiewicz-Jach, A.; Ledwa, K.A.; Piecuch, A.; Giersig, M.; Drulis-Kawa, Z.; Wiglusz, R.J. Structural modification of nanohydroxyapatite Ca₁₀(PO₄)₆(OH)₂ related to Eu³⁺ and Sr²⁺ ions doping and its spectroscopic and antimicrobial properties. *J. Inorg. Biochem.* **2020**, *203*, 110884. [[CrossRef](#)]
5. Thukkaram, M.; Cools, P.; Nikiforov, A.; Rigole, P.; Coenye, T.; Van Der Voort, P.; Du Laing, G.; Vercruyse, C.; Declercq, H.; Morent, R.; et al. Antibacterial activity of a porous silver doped TiO₂ coating on titanium substrates synthesized by plasma electrolytic oxidation. *Appl. Surf. Sci.* **2020**, *500*, 144235. [[CrossRef](#)]

6. Patel, U.; Moss, R.M.; Hossain, K.M.Z.; Kennedy, A.R.; Barney, E.R.; Ahmed, I.; Hannon, A.C. Structural and physico-chemical analysis of calcium/strontium substituted, near-invert phosphate based glasses for biomedical applications. *Acta Biomater.* **2017**, *60*, 109–127. [[CrossRef](#)]
7. Chen, F.; Liu, X. Advancing biomaterials of human origin for tissue engineering. *Prog. Polym. Sci.* **2016**, *53*, 86–168. [[CrossRef](#)]
8. Abramova, A.V.; Abramov, V.O.; Bayazitov, V.M.; Voitov, Y.; Straumal, E.A.; Lermontov, S.A.; Cherdyntseva, T.A.; Braeutigam, P.; Weiße, M.; Günther, K. A sol-gel method for applying nanosized antibacterial particles to the surface of textile materials in an ultrasonic field. *Ultrason. Sonochem.* **2020**, *60*, 104788. [[CrossRef](#)]
9. Mrówczyński, R.; Jędrzak, A.; Szutkowski, K.; Grześkowiak, B.F.; Coy, E.; Markiewicz, R.; Jesionowski, T.; Jurga, S. Cyclodextrin-based magnetic nanoparticles for cancer therapy. *Nanomaterials* **2018**, *8*, 170. [[CrossRef](#)]
10. Shane, H.L.; Lukomska, E.; Anderson, S. Topical application of the quaternary ammonium compound didecyldimethylammonium chloride activates type 2 innate lymphoid cells and initiates a mixed-type allergic response. *J. Allergy Clin. Immunol.* **2019**, *143*, AB1. [[CrossRef](#)]
11. Baek, S.; Joo, S.H.; Su, C.; Toborek, M. Antibacterial effects of graphene- and carbon-nanotube-based nanohybrids on Escherichia coli: Implications for treating multidrug-resistant bacteria. *J. Environ. Manag.* **2019**, *247*, 214–223. [[CrossRef](#)] [[PubMed](#)]
12. Durić, S.; Vojnovic, S.; Pavic, A.; Mojicevic, M.; Wadepohl, H.; Savić, N.D.; Popsavin, M.; Nikodinovic-Runic, J.; Djuran, M.; Glišić, B.D. New polynuclear 1,5-naphthyridine-silver(I) complexes as potential antimicrobial agents: The key role of the nature of donor coordinated to the metal center. *J. Inorg. Biochem.* **2020**, *203*, 110872. [[CrossRef](#)] [[PubMed](#)]
13. Sagadevan, S.; Vennila, S.; Marlinda, A.R.; Al-Douri, Y.; Johan, M.R.; Lett, J.A. Synthesis and evaluation of the structural, optical, and antibacterial properties of copper oxide nanoparticles. *Appl. Phys. A* **2019**, *125*, 489. [[CrossRef](#)]
14. Vijayan, R.; Joseph, S.; Mathew, B. Anticancer, antimicrobial, antioxidant, and catalytic activities of green-synthesized silver and gold nanoparticles using Bauhinia purpurea leaf extract. *Bioprocess Biosyst. Eng.* **2019**, *42*, 305–319. [[CrossRef](#)]
15. Chegeni, M.; Pour, S.K.; Dizaji, B.F. Synthesis and characterization of novel antibacterial sol-gel derived TiO₂/Zn₂TiO₄/Ag nanocomposite as an active agent. *Ceram. Int.* **2019**, *45*, 23857–24954. [[CrossRef](#)]
16. Matsunaga, T.; Tomoda, R.; Nakajima, T.; Wake, H. Photoelectrochemical sterilization of microbial cells by semiconductor powders. *FEMS Microbiol. Lett.* **1985**, *29*, 211–214. [[CrossRef](#)]
17. Kikuchi, Y.; Sunada, K.; Iyoda, T.; Hashimoto, K.; Fujishima, A. Photocatalytic bactericidal effect of TiO₂ thin films: Dynamic view of the active oxygen species responsible for the effect. *J. Photochem. Photobiol. A* **1997**, *106*, 51–56. [[CrossRef](#)]
18. Nadtochenko, V.; Denisov, N.; Sarkisov, O.; Gummy, D.; Pulgarin, C.; Kiwi, J. Laser kinetic spectroscopy of the interfacial charge transfer between membrane cell walls of E. coli and TiO₂. *J. Photochem. Photobiol. A* **2006**, *181*, 401–407. [[CrossRef](#)]
19. Liu, Y.; Wang, X.; Yang, F.; Yang, X. Excellent antimicrobial properties of mesoporous anatase TiO₂ and Ag/TiO₂ composite films. *Microporous Mesoporous Mater.* **2008**, *114*, 431–439. [[CrossRef](#)]
20. Lendzion-Bieluń, Z.; Wojciechowska, A.; Grzechulska-Damszel, J.; Narkiewicz, U.; Śniadecki, Z.; Idzikowski, B. Effective processes of phenol degradation on Fe₃O₄-TiO₂ nanostructured magnetic photocatalyst. *J. Phys. Chem. Solids* **2020**, *136*, 109178. [[CrossRef](#)]
21. Sun, J.; Zhou, S.; Hou, P.; Yang, Y.; Weng, J.; Li, X.; Li, M. Synthesis and characterization of biocompatible Fe₃O₄ nanoparticles. *J. Biomed. Mater. Res. A* **2006**, *80*, 333–341. [[CrossRef](#)] [[PubMed](#)]
22. Wang, W.; Zhu, Y.; Ruan, M. Microwave-assisted synthesis and magnetic property of magnetite and hematite nanoparticles. *J. Nanoparticle Res.* **2007**, *9*, 419–426. [[CrossRef](#)]
23. Chin, S.F.; Makha, M.; Raston, L.C.; Saunders, M. Magnetite ferrofluids stabilized by sulfonato-calixarenes. *Chem. Commun.* **2007**, 1948–1950. [[CrossRef](#)] [[PubMed](#)]
24. Lee, H.; Shao, H.; Huang, Y.; Kwak, B. Synthesis of MRI contrast agent by coating superparamagnetic iron oxide with chitosan. *IEEE Trans. Magn.* **2005**, *41*, 4102–4104. [[CrossRef](#)]
25. Jurgons, R.; Seliger, C.; Hilpert, A.; Trahms, L.; Odenbach, S.; Alexiou, C. Drug loaded magnetic nanoparticles for cancer therapy. *J. Phys. Condens. Matter* **2006**, *18*, 2893. [[CrossRef](#)]

26. Wang, X.; Liao, Y.; Zhang, D.; Wen, T.; Zhong, Z. A review of Fe₃O₄ thin films: Synthesis, modification and applications. *J. Mater. Sci. Technol.* **2018**, *34*, 1259–1272. [[CrossRef](#)]
27. Xu, Z.P.; Zeng, Q.H.; Lu, G.Q.; Yu, A.B. Inorganic nanoparticles as carriers for efficient cellular delivery. *Chem. Eng. Sci.* **2006**, *61*, 1027–1040. [[CrossRef](#)]
28. Ghazanfari, M.R.; Kashefi, M.; Shams, S.F.; Jaafari, M.R. Perspective of Fe₃O₄ nanoparticles role in biomedical applications. *Biochem. Res. Int.* **2016**, *2016*, 7840161. [[CrossRef](#)]
29. Wang, J.; Zheng, S.; Shao, Y.; Liu, J.; Xu, Z.; Zhu, D. Amino-functionalized Fe₃O₄@SiO₂ core-shell magnetic nanomaterial as a novel adsorbent for aqueous heavy metals removal. *J. Colloid Interface Sci.* **2010**, *349*, 293–299. [[CrossRef](#)]
30. Fan, F.L.; Qin, Z.; Bai, J.; Rong, W.D.; Fan, F.Y.; Tian, W.; Wu, X.L.; Wang, Y.; Zhao, L. Rapid removal of uranium from aqueous solutions using magnetic Fe₃O₄@SiO₂ composite particles. *J. Environ. Radioact.* **2012**, *106*, 40–46. [[CrossRef](#)] [[PubMed](#)]
31. Zhu, Y.; Ikoma, T.; Hanagata, N.; Kaskel, S. Rattle-type Fe₃O₄@SiO₂ hollow mesoporous spheres as carriers for drug delivery. *Small* **2010**, *6*, 471–478. [[CrossRef](#)] [[PubMed](#)]
32. Shao, M.; Ning, F.; Zhao, J.; Wei, M.; Evans, D.G.; Duan, X. Preparation of Fe₃O₄@SiO₂@layered double hydroxide core-shell microspheres for magnetic separation of proteins. *J. Am. Chem. Soc.* **2012**, *134*, 1071–1077. [[CrossRef](#)] [[PubMed](#)]
33. Wu, K.; Jing, C.; Zhang, J.; Liu, T.; Yang, S.; Wang, W. Magnetic Fe₃O₄@CuO nanocomposite assembled on graphene oxide sheets for the enhanced removal of arsenic (III/V) from water. *Appl. Surf. Sci.* **2018**, *466*, 746–756. [[CrossRef](#)]
34. Zhang, Y.; Qiu, L.; Yuan, Y.; Zhu, Y.; Jiang, X.; Xiao, J. Magnetic Fe₃O₄@C/Cu and Fe₃O₄@CuO core-shell composites constructed from MOF-based materials and their photocatalytic properties under visible light. *Applied Catal. B Environ.* **2014**, *144*, 863–869. [[CrossRef](#)]
35. Vinosel, V.M.; Anand, S.; Janifer, M.A.; Pauline, S. Photocatalytic and antibacterial applications of magnetic Fe₃O₄-CuO nanocomposite. *Mater. Today Proc.* **2019**, *8*, 301–309. [[CrossRef](#)]
36. Rajabi, S.K.; Sohrabnezhad, S.; Ghafourian, S. Fabrication of Fe₃O₄@CuO core-shell from MOF based materials and its antibacterial activity. *J. Solid State Chem.* **2016**, *244*, 160–163. [[CrossRef](#)]
37. Raza, A.; Shen, H.; Haidry, A.A.; Cui, S. Hydrothermal synthesis of Fe₃O₄/TiO₂/g-C₃N₄: Advanced photocatalytic application. *Appl. Surf. Sci.* **2019**, *488*, 887–895. [[CrossRef](#)]
38. Mehdipour, M.; Pirbazari, A.E.; Khayati, G. Cobalt photodeposition on Fe₃O₄/TiO₂ as a novel magnetically separable visible-light-driven photocatalyst for efficient degradation of 2,4-dichlorophenol. *Desalination Water Treat.* **2019**, *155*, 329–340. [[CrossRef](#)]
39. Zabihisahebi, A.; Koushkbaghi, S.; Pishnamazi, M.; Askari, A.; Khosravi, R.; Irani, M. Synthesis of cellulose acetate/chitosan/SWCNT/Fe₃O₄/TiO₂ composite nano fibers for the removal of Cr(VI), As(V), Methylene blue and Congo red from aqueous solutions. *Int. J. Biol. Macromol.* **2019**, *140*, 1296–1304. [[CrossRef](#)]
40. Beduk, F. Superparamagnetic nanomaterial Fe₃O₄-TiO₂ for the removal of As(V) and As(III) from aqueous solutions. *Environ. Technol.* **2016**, *37*, 1790–1801. [[CrossRef](#)]
41. Zeng, L.; Ren, W.; Xiang, L.; Zheng, J.; Chen, B.; Wu, A. Multifunctional Fe₃O₄-TiO₂ nanocomposites for magnetic resonance imaging and potential photodynamic therapy. *Nanoscale* **2013**, *5*, 2107–2113. [[CrossRef](#)]
42. Arabzadeh, N.; Mohammadi, A.; Darwish, M.; Abuzerr, S. Construction of a TiO₂-Fe₃O₄-Decorated molecularly imprinted polymer nanocomposite for tartrazine degradation: Response surface methodology modeling and optimization. *J. Chinese Chem. Soc.* **2019**, *66*, 474–483. [[CrossRef](#)]
43. Babudurai, M.; Hernandez-Maya, R.; Solís, M.; Th-Th, C.; Velumani, S. Photocatalytic degradation of Orange G using TiO₂/Fe₃O₄ nanocomposites. *J. Mater. Sci. Mater. Electron.* **2018**, *29*, 15436–15444. [[CrossRef](#)]
44. Salamat, S.; Younesi, H.; Bahramifar, N. Synthesis of magnetic core-shell Fe₃O₄@TiO₂ nanoparticles from electric arc furnace dust for photocatalytic degradation of steel mill wastewater. *RSC Adv.* **2017**, *7*, 19391–19405. [[CrossRef](#)]
45. Kermani, M.; Kakavandi, B.; Farzadkia, M.; Esrafil, A.; Jokandan, S.F.; Shahsavani, A. Catalytic ozonation of high concentrations of catechol over TiO₂@Fe₃O₄ magnetic core-shell nanocatalyst: Optimization, toxicity and degradation pathway studies. *J. Clean. Prod.* **2018**, *192*, 597–607. [[CrossRef](#)]
46. Li, Y.; Zhang, M.; Guo, M.; Wang, X. Preparation and properties of a nano TiO₂/Fe₃O₄ composite superparamagnetic photocatalyst. *Rare Met.* **2009**, *28*, 423–427. [[CrossRef](#)]

47. Li, Z.Q.; Wang, H.L.; Zi, L.Y.; Zhang, J.J.; Zhang, Y.S. Preparation and photocatalytic performance of magnetic TiO₂-Fe₃O₄/graphene (RGO) composites under VIS-light irradiation. *Ceram. Int.* **2015**, *41*, 10634–10643. [[CrossRef](#)]
48. Bui, V.K.H.; Park, D.; Pham, T.N.; An, Y.; Choi, J.S.; Lee, H.U.; Kwon, O.H.; Moon, J.Y.; Kim, K.T.; Lee, Y.C. Synthesis of MgAC-Fe₃O₄/TiO₂ hybrid nanocomposites via sol-gel chemistry for water treatment by photo-Fenton and photocatalytic reactions. *Sci. Rep.* **2019**, *9*, 1–11. [[CrossRef](#)]
49. Beketova, D.; Motola, M.; Sopha, H.; Michalicka, J.; Cicmancova, V.; Dvorak, F.; Hromadko, L.; Frumarova, B.; Stoica, M.; Macak, J.M. One-step decoration of TiO₂ nanotubes with Fe₃O₄ nanoparticles: Synthesis and photocatalytic and magnetic properties. *ACS Appl. Nano Mater.* **2020**, *3*, 1553–1563. [[CrossRef](#)]
50. Rodríguez-Carvajal, J. Recent advances in magnetic structure determination by neutron powder diffraction. *Phys. B* **1993**, *192*, 55–69. [[CrossRef](#)]
51. CLSI. *Performance Standards for Antimicrobial Susceptibility Testing*, 29th ed.; CLSI supplement M100; Clinical and Laboratory Standards Institute: Wayne, PA, USA, 2019.
52. ASTM. *E2149—01 Standard Methods for Determining the Antimicrobial Activity of Immobilized Antimicrobial Agents under Dynamic Contact Conditions*; ASTM International: West Conshohocken, PA, USA, 2008.
53. Karatutlu, A.; Barhoum, A.; Sapelkin, A. Theories of nanoparticle and nanostructure formation in liquid phase. In *Emerging Applications of Nanoparticles and Architecture Nanostructures*; Barhoum, A., Makhlouf, A.S.H., Eds.; Elsevier Inc.: Amsterdam, The Netherlands, 2018; pp. 597–619. [[CrossRef](#)]
54. Wang, P.; Yi, Q.; Xing, M.; Zhang, J. Selective synthesis of TiO₂ single nanocrystals and titanate nanotubes: A controllable atomic arrangement approach via NH₄TiOF₃ mesocrystals. *Phys. Chem. Chem. Phys.* **2015**, *17*, 21982–21987. [[CrossRef](#)] [[PubMed](#)]
55. Martínez-Mera, I.; Espinosa-Pesqueira, M.E.; Pérez-Hernández, R.; Arenas-Alatorre, J. Synthesis of magnetite (Fe₃O₄) nanoparticles without surfactants at room temperature. *Mater. Lett.* **2007**, *61*, 4447–4451. [[CrossRef](#)]
56. Jędrzak, A.; Rębiś, T.; Kuznowicz, M.; Jesionowski, T. Bio-inspired magnetite/lignin/polydopamine-glucose oxidase biosensing nanoplatform. From synthesis, via sensing assays to comparison with others glucose testing techniques. *Int. J. Biol. Macromol.* **2019**, *127*, 677–682. [[CrossRef](#)]
57. Siwińska-Stefańska, K.; Zdarta, J.; Paukszta, D.; Jesionowski, T. The influence of addition of a catalyst and chelating agent on the properties of titanium dioxide synthesized via the sol-gel method. *J. Sol. Gel Sci. Technol.* **2015**, *75*, 264–278. [[CrossRef](#)]
58. Siwińska-Stefańska, K.; Ciesielczyk, F.; Kołodziejczak-Radzimska, A.; Paukszta, D.; Sójka-Ledakowicz, J.; Jesionowski, T. TiO₂-SiO₂ inorganic barrier composites: From synthesis to application. *Pigment Resin Technol.* **2012**, *41*, 139–148. [[CrossRef](#)]
59. Tan, L.; Zhang, X.; Liu, Q.; Jing, X.; Liu, J.; Song, D.; Hu, S.; Liu, L.; Wang, J. Synthesis of Fe₃O₄/TiO₂ core-shell magnetic composites for highly efficient sorption of uranium (VI). *Colloids Surf. A Physicochem. Eng. Asp.* **2015**, *469*, 279–286. [[CrossRef](#)]
60. Khashan, S.; Dagher, S.; Tit, N.; Alazzam, A.; Obaidat, I. Novel method for synthesis of Fe₃O₄@TiO₂ core/shell nanoparticles. *Surf. Coat. Technol.* **2017**, *322*, 92–98. [[CrossRef](#)]
61. Zhu, L.; Zhang, M.; Qiao, Y.; Xiao, G.; Zhang, F.; Chen, Y. Fe₃O₄/TiO₂ core/shell nanotubes: Synthesis and magnetic and electromagnetic wave absorption characteristics. *J. Phys. Chem. C* **2010**, *114*, 16229–16235. [[CrossRef](#)]
62. Chen, C.T.; Chen, Y.C. Fe₃O₄/TiO₂ core/shell nanoparticles as affinity probes for the analysis of phosphopeptides using TiO₂ surface-assisted laser desorption/ionization mass spectrometry. *Anal. Chem.* **2005**, *77*, 5912–5919. [[CrossRef](#)] [[PubMed](#)]
63. Feizpoor, S.; Habibi-yangjeh, A. Ternary TiO₂/Fe₃O₄/CoWO₄ nanocomposites: Novel magnetic visible-light-driven photocatalysts with substantially enhanced activity through p-n heterojunction. *J. Colloid Interface Sci.* **2018**, *524*, 325–336. [[CrossRef](#)]
64. Shojei, A.F.; Shams-Nateri, A.; Ghomashpasand, M. Comparative study of photocatalytic activities of magnetically separable WO₃/TiO₂/Fe₃O₄ nanocomposites and TiO₂, WO₃/TiO₂ and TiO₂/Fe₃O₄ under visible light irradiation. *Superlattices Microstruct.* **2015**, *88*, 211–224. [[CrossRef](#)]
65. Li, X.; Cui, M.; Lee, Y.; Choi, J.; Khim, J. Application of pea-like yolk-shell structured Fe₃O₄@TiO₂ nanosheets for photocatalytic and photo-fenton oxidation of bisphenol-A. *RSC Adv.* **2019**, *9*, 22153–22160. [[CrossRef](#)]

66. Shojaie, A.; Fattahi, M.; Jorfi, S.; Ghasemi, B. Synthesis and evaluations of Fe₃O₄-TiO₂-Ag nanocomposites for photocatalytic degradation of 4-chlorophenol (4-CP): Effect of Ag and Fe compositions. *Int. J. Ind. Chem.* **2018**, *9*, 141–151. [[CrossRef](#)]
67. Fisli, A.; Saridewi, R.; Dewi, S.H.; Gunlazuardi, J. Preparation and characterization of Fe₃O₄/TiO₂ composites by heteroagglomeration. *Adv. Mater. Res.* **2013**, *626*, 131–137. [[CrossRef](#)]
68. Bruvera, I.J.; Mendoza Zélis, P.; Pilar Calatayud, M.; Goya, G.F.; Sánchez, F.H. Determination of the blocking temperature of magnetic nanoparticles: The good, the bad, and the ugly. *J. Appl. Phys.* **2015**, *118*, 184304. [[CrossRef](#)]
69. Walz, F. The Verwey transition—A topical review. *J. Phys. Condens. Matter* **2002**, *14*, 285–340. [[CrossRef](#)]
70. Yang, J.B.; Zhou, X.D.; Yelon, W.B.; James, W.J.; Cai, Q.; Gopalakrishnan, K.V.; Malik, S.K.; Sun, X.C.; Nikles, D.E. Magnetic and structural studies of the Verwey transition in Fe_{3-δ}O₄ nanoparticles. *J. Appl. Phys.* **2004**, *95*, 7540–7542. [[CrossRef](#)]
71. Mitra, A.; Mohapatra, J.; Meena, S.S.; Tomy, C.V.; Aslam, M. Verwey transition in ultrasmall-sized octahedral Fe₃O₄ nanoparticles. *J. Phys. Chem. C* **2014**, *118*, 19356–19362. [[CrossRef](#)]
72. Lee, J.; Kwon, S.G.; Park, J.G.; Hyeon, T. Size dependence of metal-insulator transition in stoichiometric Fe₃O₄ nanocrystals. *Nano Lett.* **2015**, *15*, 4337–4342. [[CrossRef](#)]
73. Nedelkoski, Z.; Kepaptsoglou, D.; Lari, L.; Wen, T.; Booth, R.A.; Oberdick, S.D.; Galindo, P.L.; Ramasse, Q.M.; Evans, R.F.L.; Majetich, S.; et al. Origin of reduced magnetization and domain formation in small magnetite nanoparticles. *Sci. Rep.* **2017**, *7*, 1–8. [[CrossRef](#)]
74. Chauvet, O.; Forro, L.; Kos, I.; Miljak, M. Magnetic properties of the anatase phase of TiO₂. *Solid State Commun.* **1995**, *93*, 667–669. [[CrossRef](#)]
75. Majetich, S.A.; Wen, T.; Mefford, O.T. Magnetic nanoparticles. *MRS Bull.* **2013**, *38*, 899–903. [[CrossRef](#)]
76. Mohapatra, J.; Xing, M.; Liu, J.P. Inductive thermal effect of ferrite magnetic nanoparticles. *Materials* **2019**, *12*, 3208. [[CrossRef](#)] [[PubMed](#)]
77. Kumar, P.M.; Badrinarayanan, S.; Sastry, M. Nanocrystalline TiO₂ studied by optical, FTIR and X-ray photoelectron spectroscopy: Correlation to presence of surface states. *Thin Solid Films* **2000**, *358*, 122–130. [[CrossRef](#)]
78. Wu, L.; Yu, J.C.; Zhang, L.; Wang, X.; Ho, W. Preparation of a highly active nanocrystalline TiO₂ photocatalyst from titanium oxo cluster precursor. *J. Solid State Chem.* **2004**, *177*, 2584–2590. [[CrossRef](#)]
79. Cheng, F.Y.; Su, C.H.; Yang, Y.S.; Yeh, C.S.; Tsai, C.Y.; Wu, C.L.; Wu, M.T.; Shieh, D.B. Characterization of aqueous dispersions of Fe₃O₄ nanoparticles and their biomedical applications. *Biomaterials* **2005**, *26*, 729–738. [[CrossRef](#)]
80. Chan, C.C.; Chang, C.C.; Hsu, C.W.; Wang, S.K.; Lin, J. Photocatalytic activities of Pd-loaded mesoporous TiO₂ thin films. *Chem. Eng. J.* **2009**, *152*, 492–497. [[CrossRef](#)]
81. Jędrzak, A.; Rębiś, T.; Nowicki, M.; Synoradzki, K.; Mrówczyński, R.; Jesionowski, T. Polydopamine grafted on an advanced Fe₃O₄/lignin hybrid material and its evaluation in biosensing. *Appl. Surf. Sci.* **2018**, *455*, 455–464. [[CrossRef](#)]
82. Raghunath, A.; Perumal, E. Metal oxide nanoparticles as antimicrobial agents: A promise for the future. *Int. J. Antimicrob. Agents* **2017**, *49*, 137–152. [[CrossRef](#)]
83. Sievers, N.V.; Pollo, L.D.; Corção, G.; Medeiros Cardozo, N.S. In situ synthesis of nanosized TiO₂ in polypropylene solution for the production of films with antibacterial activity. *Mater. Chem. Phys.* **2020**, *246*, 122824. [[CrossRef](#)]
84. Yildiz, A.; Vatanserver Bayramol, D.; Atav, R.; Ağırgan, A.Ö.; Aydın Kurç, M.; Ergünay, U.; Mayer, C.; Hadimani, R.L. Synthesis and characterization of Fe₃O₄@Cs@Ag nanocomposite and its use in the production of magnetic and antibacterial nanofibrous membranes. *Appl. Surf. Sci.* **2020**, *521*, 146332. [[CrossRef](#)]
85. Tseng, W.J.; Chuang, Y.C.; Chen, Y.A. Mesoporous Fe₃O₄@Ag@TiO₂ nanocomposite particles for magnetically recyclable photocatalysis and bactericide. *Adv. Powder Technol.* **2018**, *29*, 664–671. [[CrossRef](#)]
86. Cheng, T.C.; Yao, K.S.; Yeh, N.; Chang, C.I.; Hsu, H.C.; Chien, Y.T.; Chang, C.Y. Visible light activated bactericidal effect of TiO₂/Fe₃O₄ magnetic particles on fish pathogens. *Surf. Coat. Technol.* **2009**, *204*, 1141–1144. [[CrossRef](#)]
87. Ma, S.; Zhan, S.; Jia, Y.; Zhou, Q. Superior Antibacterial Activity of Fe₃O₄-TiO₂ nanosheets under solar light. *ACS Appl. Mater. Interfaces* **2015**, *7*, 21875–21883. [[CrossRef](#)]

88. Xu, J.W.; Gao, Z.D.; Han, K.; Liu, Y.; Song, Y.Y. Synthesis of magnetically separable $\text{Ag}_3\text{PO}_4/\text{TiO}_2/\text{Fe}_3\text{O}_4$ heterostructure with enhanced photocatalytic performance under visible light for photoinactivation of bacteria. *ACS Appl. Mater. Interfaces* **2014**, *6*, 15122–15131. [[CrossRef](#)]
89. Li, C.; Younesi, R.; Cai, Y.; Zhu, Y.; Ma, M.; Zhu, J. Photocatalytic and antibacterial properties of Au-decorated $\text{Fe}_3\text{O}_4/\text{TiO}_2$ core-shell microspheres. *Appl. Catal. B Environ.* **2014**, *156*, 314–322. [[CrossRef](#)]
90. Foster, H.A.; Ditta, I.B.; Varghese, S.; Steele, A. Photocatalytic disinfection using titanium dioxide: Spectrum and mechanism of antimicrobial activity. *Appl. Microbiol. Biotechnol.* **2011**, *90*, 1847–1868. [[CrossRef](#)]
91. Van Houdt, R.; Michiels, C.W. Role of bacterial cell surface structures in *Escherichia coli* biofilm formation. *Res. Microbiol.* **2005**, *156*, 626–633. [[CrossRef](#)]
92. Li, W.R.; Xie, X.B.; Shi, Q.S.; Duan, S.S.; Ouyang, Y.S.; Chen, Y.B. Antibacterial effect of silver nanoparticles on *Staphylococcus aureus*. *Biomaterials* **2011**, 135–141. [[CrossRef](#)]
93. Kuhn, S.; Slavetinsky, C.J.; Peschel, A. Synthesis and function of phospholipids in *Staphylococcus aureus*. *Int. J. Med. Microbiol.* **2015**, *305*, 196–202. [[CrossRef](#)]

Publisher’s Note: MDPI stays neutral with regard to jurisdictional claims in published maps and institutional affiliations.



© 2020 by the authors. Licensee MDPI, Basel, Switzerland. This article is an open access article distributed under the terms and conditions of the Creative Commons Attribution (CC BY) license (<http://creativecommons.org/licenses/by/4.0/>).